

## Hybrid broadband strong-motion simulation to investigate the near-source characteristics of the M6.5, 30 October 2016 Norcia, Italy earthquake

Javier Ojeda <sup>a,\*</sup>, Aybige Akinci <sup>b</sup>, Elisa Tinti <sup>c,b</sup>, Sebastian Arriola <sup>d</sup>, Sergio Ruiz <sup>a</sup>

<sup>a</sup> Departamento de Geofísica, Universidad de Chile, Blanco Encalada, 2002, Santiago, Chile

<sup>b</sup> Istituto Nazionale di Geofisica e Vulcanologia, via di Vigna Murata 605, Rome, 00143, Italy

<sup>c</sup> Università La Sapienza, piazzale Aldo Moro, Rome, 00185, Italy

<sup>d</sup> Centro Sismológico Nacional, Universidad de Chile, Blanco Encalada, 2002, Santiago, Chile



### ARTICLE INFO

**Keywords:**

Ground-motion simulation  
Hybrid method  
Norcia M6.5 earthquake  
Site effects

### ABSTRACT

During the 2016–2017 Central Italy earthquake sequence, a series of moderate to large earthquakes  $M > 5$  occurred near the Amatrice and Norcia towns. These events are recorded on a dense seismic network, providing relevant observational evidence of complex earthquakes in time and space. In this work, we used this substantial data set to study the ground-motion characteristics of the Norcia earthquake M6.5 on October 30, 2016, through a broadband ground-motion simulation. Three-component broadband seismograms are generated to cover the entire frequency band of engineering interest. Low and high frequencies are computed considering the heterogeneous slip rupture model of Scognamiglio et al. (2018) [1]. High frequencies are calculated using a stochastic approach including P, SV, and SH waves, while low frequencies are obtained through a forward simulation of the kinematic model at the various stations. To predict earthquake-induced ground-motions in the area, we adopted region-specific attenuation and source scaling parameters derived by Malagnini et al. (2011) [2]. Ground-motion parameters, including peak ground acceleration (PGA), peak ground velocity (PGV) and spectral amplitudes, are calculated at the selected sites adopting physics-based parameters to understand better the earthquake fault rupture, the wave propagation, and their impacts on the seismic hazard assessment in the region. We showed that combining the fault rupture history over the entire frequency spectrum of engineering interest, the attenuation characteristics of the seismic wave propagation and the properly defined site responses can improve the prediction of ground-motions and time histories, especially in near seismic sources.

### 1. Introduction

The Central Apennines belt is one of the most seismically active regions in Italy, with the frequent occurrence of strong ( $M > 6.0$ ) destructive earthquakes. The region was formed in the Miocene to Pliocene under the ongoing subduction environment where the Adriatic Plate collides with and plunges beneath the Eurasian Plate [3]. As a consequence of this process thrust belts in the Adriatic coast and extension structures in the axial sector of the belt produced a broad and complex normal faults system elongated in the NW-SE direction [4]. Recently, a series of damaging earthquakes, M6.0 on August 24, M5.9 on October 26, and M6.5 on October 30, 2016, occurred near the town of Amatrice and Norcia in the Central Apennines. The Norcia earthquake, the largest event of the sequence, occurred just a few tens of kilometers

north-west of the L'Aquila (Abruzzo) area, which was hit by the M6.3 earthquake on April 6, 2009. These earthquakes have increased attention to seismic hazard, engineering applications, and earthquake risk mitigation efforts in the region.

For these reasons, in such areas, simulated ground-motions may help to understand the earthquake characteristics for both seismological and earthquake engineering purposes. Physically-based ground-motion simulation and verification are the keys and basic tasks for establishing its predictive capabilities in seismic risk assessment and seismic engineering applications. Moreover, the complete time series of ground-motion simulations from 0.02 Hz up to frequencies of 10 Hz are needed for Civil engineers to design earthquake-resistant structures and retrofit vulnerable existing structures (e.g. Ref. [5]).

Earthquakes generate broadband ground-motions, which include

\* Corresponding author.

E-mail addresses: [ojeda@dgf.uchile.cl](mailto:ojeda@dgf.uchile.cl) (J. Ojeda), [aybige.akinci@ingv.it](mailto:aybige.akinci@ingv.it) (A. Akinci), [elisa.tinti@uniroma1.it](mailto:elisa.tinti@uniroma1.it) (E. Tinti), [seba.arriola.s@gmail.com](mailto:seba.arriola.s@gmail.com) (S. Arriola), [sruiz@uchile.cl](mailto:sruiz@uchile.cl) (S. Ruiz).

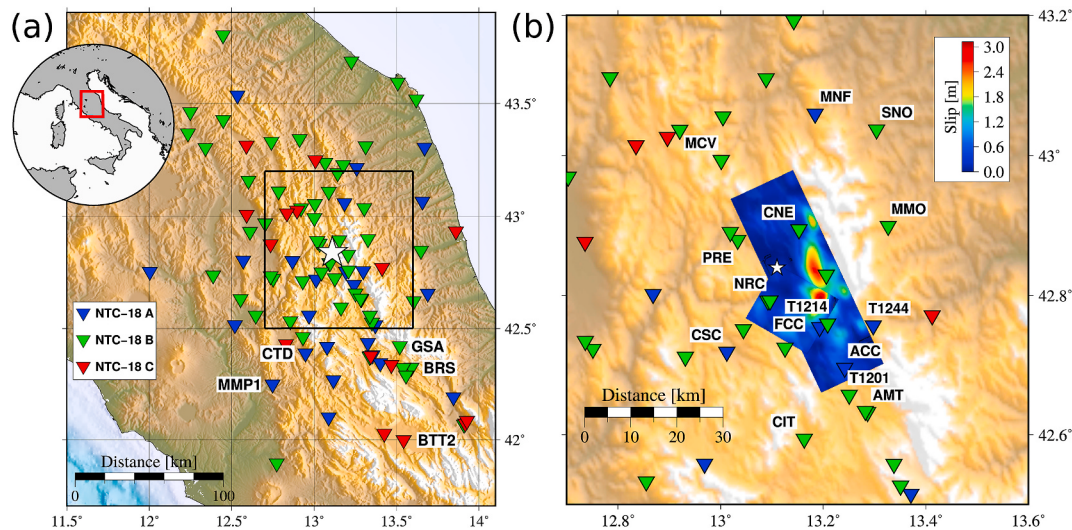


**Fig. 1.** Study area in Central Italy. (a) The epicenter of the Norcia M6.5 October 30, 2016 earthquake is represented by a white star. The strong-motion stations used in this study belong to the RAN and RSN networks are marked by triangles. Symbol color is related to site classification according to NTC-18 on the basis of the  $V_{S30}$  parameter. (b) Near-source stations and the slip distribution model of the Norcia earthquake. (For interpretation of the references to color in this figure legend, the reader is referred to the Web version of this article.)

both low ( $f < 1$  Hz) and high frequencies ( $f > 1$  Hz). However, the whole three-components waveform simulations are still challenging, especially at frequencies larger than 1 Hz. Ground-motion simulations have been refined along with developments on mathematical and computational tools and detailed regional seismological models (e.g. Refs. [6–9]). Many methods have been proposed to simulate realistic ground-motion, one of them is a hybrid method, which combines low-frequency seismograms and high-frequency ones, and is currently popular in recent studies (e.g. Refs. [10–14]).

The low-frequency part of the ground-motions is mostly simulated using deterministic and numerical methods in time or frequency domain (e.g. Refs. [15–18]) and most cases are limited to 1 Hz due to the site effects and the resolution of the adopted velocity structure. Stochastic methods are often used to account for independent random phases of motion on higher frequency bands ( $f > 1$  Hz) [19]. The most commonly used approach proposed by Boore [20] is the stochastic point-source modeling, which was further modified by Beresnev and Atkinson [21] for finite-fault effects, where each sub-fault is considered as a stochastic point source. The stochastic finite-fault modeling has been upgraded by adding the dynamic corner frequency [22]. Otarola and Ruiz [23] further improved the stochastic generation of seismograms for a stratified velocity model, including more physical parameters for simulations such as the incident and azimuthal angles, free surface factors, and energy partition for the P and SV waves. These approaches allow us to simulate three-component seismograms instead of one generic horizontal seismogram by using only SH waves. Herein, we concentrated on the Norcia M6.5 earthquake and generated broadband seismograms by adopting a hybrid method. Low-frequency seismograms are calculated using a non-negative, least-squares inversion method with simultaneous smoothing and damping implemented by Dreger et al. [24]. The high-frequency seismograms including P, SV and SH waves, were produced using the improved stochastic approach of Otarola and Ruiz [23] and Ruiz et al. [25]. In these works, an average radiation pattern derived from analytical expressions was used, as is usual in this type of simulation. Here, we calculated the radiation coefficients for each sub-fault according to the formulation proposed by Aki and Richards [26]. The

generic rock soil amplification curves [27], together with the soil amplification transfer functions for P, SV, and SH waves are implemented to improve the simulation of the three-components of accelerograms on the ground surface. Finally, broadband synthetic time series were composed by merging the low and high-frequency seismograms with a variable crossover frequency around 0.5–0.8 Hz depending on the plateau level of the spectral amplitudes [28].

In this study, we adopted region-specific physics-based input parameters related to the source and wave propagation to accurately build the earthquake rupture scenario, estimating three-components realistic time series, absolute ground-motion level, frequency content signal duration, and spatial distribution of simulated ground-motions. The simulated seismograms at the selected stations are compared against the corresponding observed ones in terms of complete ground-motion time histories, Fourier amplitude spectra (FAS), and Pseudo-spectral accelerations (PSA) with a 5% damping ratio to test and to improve the efficiency and performance of our simulations. The performances of the hybrid broadband ground-motion simulations and the predictive capability of the adopted method are discussed in terms of residuals between simulations and observations, together with empirical ground-motion models in the proximity of the epicenter. The velocity-depth profiles are considered when available from the surface to the hard rock to determine the site responses by the soil amplification transfer function approximation, including fundamental resonant peaks.

## 2. Study area and strong ground-motion data

On October 30, 2016, the Norcia earthquake occurred in the Central Apennines, a mountain range in an extensional regime related to the Tyrrhenian back-arc basin's opening and the subduction roll-back. A Quaternary NE-SW characterizes active tectonic deformation-oriented extensional regime overprinting NE-verging thrust sheets, Meso-Cenozoic carbonate rocks and Miocene flysch deposits [29]. The activated main fault is mostly normal in this region where the extension is attuned by a complex set of NW-SE and NNW-SSE striking, mostly SW dipping normal fault systems. The geologic slip rates are ranging

**Table 1**

Peak ground accelerations and velocities from the processed recordings of the October 30, 2016 Norcia earthquake, Italy, on the strong motion stations up to 30 km  $R_{jb}$  distances and local site conditions ( $V_{S30}$ ) parameters are defined according to EC8 and in the ITACA database (ITalian ACcelerometric Archive).

Station Code	Lat (°)	Lon (°)	dist (km)	$PGA_N$ (cm/s <sup>2</sup> )	$PGA_E$ (cm/s <sup>2</sup> )	$PGA_Z$ (cm/s <sup>2</sup> )	$PGV_N$ (cm/s)	$PGV_E$ (cm/s)	$PGV_Z$ (cm/s)	EC8	$V_{S30}$ (m/s)
ACC	42.696	13.242	0	387.15	456.00	561.14	38.50	42.15	21.63	A	828
FCC	42.755	13.193	0	847.80	1008.31	841.37	44.83	69.25	52.75	A	917
CLO	42.829	13.206	0	614.99	406.93	744.12	52.92	60.70	73.44	B	425
CNE	42.894	13.153	0	302.91	433.14	586.12	23.90	42.05	17.85	B	572
T1214	42.760	13.209	0	431.99	665.85	618.15	73.10	24.43	14.83	B	759
T1201	42.657	13.251	1	467.79	355.83	224.24	41.38	54.99	27.28	B	400
NRC	42.793	13.096	1.21	324.51	441.99	365.02	38.24	45.24	21.56	B	594
NOR	42.792	13.092	1.52	312.78	307.61	271.52	43.23	52.98	25.77	B	406
T1299	42.634	13.282	1.72	466.39	450.27	313.68	27.99	23.01	23.07	B	631
T1244	42.757	13.298	1.78	188.33	278.34	339.17	27.10	21.64	18.96	A	923
PRE	42.879	13.033	1.81	310.95	257.24	200.00	15.96	11.19	6.72	B	–
AMT	42.632	13.286	2.04	425.43	565.02	322.51	31.21	29.48	31.78	B	559
T1213	42.725	13.126	2.22	874.74	802.73	828.15	33.54	49.62	30.29	B	576
T1216	42.891	13.019	2.34	264.21	256.49	161.91	13.28	13.62	6.48	A	807
CIT	42.594	13.163	5.83	211.92	333.05	140.86	14.34	16.51	8.99	B	443
T1212	42.752	13.045	6.97	252.60	269.73	166.05	24.01	24.65	12.70	B	537
MCV	42.993	13.001	9.63	365.42	307.65	433.39	11.27	7.43	6.73	B	575
MMO	42.899	13.327	10.60	192.27	194.03	143.57	13.93	10.88	10.49	B	787
CSC	42.719	13.012	10.89	155.07	160.18	161.47	10.48	11.70	6.04	A	1043
ACT	42.771	13.413	10.93	386.88	257.26	260.03	10.40	5.27	6.38	C	–
PCB	42.558	13.338	11.32	241.76	138.04	59.12	9.00	9.28	8.21	B	659
MNF	43.060	13.184	12.55	114.64	126.19	106.50	7.00	7.00	6.06	A	989
MSC	42.527	13.351	14.91	95.58	93.81	49.32	9.21	8.15	8.26	B	743
MSCT	42.527	13.351	14.92	99.06	98.02	51.78	9.46	8.49	8.52	B	740
T1219	43.056	13.005	15.79	264.57	156.21	145.76	9.73	6.14	6.81	B	551
SNO	43.037	13.304	15.81	115.66	80.75	70.73	6.46	6.60	5.29	B	442
SPD	42.515	13.371	16.78	106.00	77.68	47.53	7.80	6.72	7.33	A	966
CLF	43.037	12.920	17.00	164.81	114.86	94.79	9.82	10.70	5.75	B	370
T1217	42.712	12.931	17.22	111.26	107.68	93.16	7.87	4.19	5.33	B	788
FOC	43.026	12.897	17.30	333.05	370.75	224.58	7.18	12.20	4.84	C	342
T1215	42.802	12.869	17.64	85.84	76.19	64.05	4.68	6.99	4.52	A	949
T1220	43.110	13.089	18.59	258.52	234.42	142.52	15.69	16.33	7.79	B	717
FOS	43.015	12.835	20.21	119.21	83.97	50.94	6.06	5.31	2.85	C	334
LSS	42.558	12.969	21.65	53.05	44.44	41.03	3.73	3.96	3.70	A	1258
TERO	42.623	13.604	22.88	122.23	87.49	57.19	8.58	6.20	3.66	B	–
PZI1	42.436	13.326	23.26	58.00	68.88	30.30	6.93	5.82	5.24	A	855
TRE	42.877	12.736	24.96	122.42	120.71	65.71	8.71	6.65	4.50	C	353
ANT	42.418	13.079	25.99	49.25	41.59	23.91	6.09	6.54	2.63	A	896
MDAR	43.193	13.143	27.05	69.81	88.08	58.99	4.22	4.49	2.62	B	611
FOPC	42.970	12.703	28.12	93.00	114.08	51.38	4.98	6.90	3.03	B	465
TER	42.657	13.690	29.34	81.43	75.74	40.29	7.58	4.76	3.73	A	888
TRL	42.461	12.932	29.76	97.32	70.69	32.51	7.85	8.23	2.59	B	652

between 0.5 and 1.3 mm/year [30,31], while the total rate of extension is varying between 1.0 and 3.0 mm/year based on the geodetic observations [32,33].

The October 30, 2016 Norcia event affected about 400 km<sup>2</sup> wide area with a length of nearly 46 km along with the Mt. Vettore - Mt. Bove fault system. It nucleated in the area between the two previous moderate events (M6.0 on August 24, 2016 and M5.9 on October 26, 2016) and filled the gap between the previous ruptures. The focal mechanism of the largest earthquake is consistent with the normal faulting of most aftershocks, in agreement with the extension of the Apennines region [34,35].

In the last three decades, two other important seismic sequences occurred in the area, each characterized by their main event: the 1997 Colfiorito event, M6.0, and the 2009 L'Aquila event, M6.3. All of these events, including major earthquakes in the 2016–2017 seismic sequence, produced several ruptures on the surface along the main NW-SE-striking extensional faults [36,37] and caused significant structural failures, leading to thousands of injuries and the loss of hundreds of lives.

The 2016 Norcia earthquake was recorded by 73 strong-motion stations within an epicentral distance of 50 km, with good azimuthal coverage (Fig. 1). In Table 1, the strong-ground-motion stations are given, with necessary information presenting the station name, location, site class according to the Italian Seismic Design Codes NTC-18 classification, source-to-site distances, and peak ground acceleration (PGA)

and peak ground velocity (PGV) values in both north-south (NS) and east-west (EW) directions. The processed acceleration-time histories of the selected stations are taken from the Italian Strong-Motion Network managed by the Department of Civil Protection (RAN) and the Italian Seismic Network (Rete Sismica Nazionale, RSN) managed by the Istituto Nazionale di Geofisica e Vulcanologia (INGV). In this study, we considered 98 sites, which belong to RAN and RSN networks, and some of them are from temporary local networks. Fig. 1a shows these stations and the epicenter of the Norcia earthquake. Symbol color is related to site classification according to NTC-18 based on the  $V_{S30}$  parameter.

In the study region, we used the 1D velocity model presented in Herrmann et al. [38] for Central Italy. For some strong-motion stations, the velocity-depth profiles were available down to the engineering bedrock, and for the rest of the stations we used both the average shear wave velocity of the top 30 m of the soil profile,  $V_{S30}$ , and the site classifications according to the Italian seismic design code (NTC-18).

### 3. Methodology to generate broadband synthetic seismograms

We performed three-component broadband synthetic records covering the entire frequency band of engineering interest. These time series were composed by merging the low (LF) and high-frequency (HF) seismograms with a variable crossover frequency depending on the wavelength resolution. Following the procedure of Mai and Beroza [28], the two simulation techniques' results are combined into the frequency

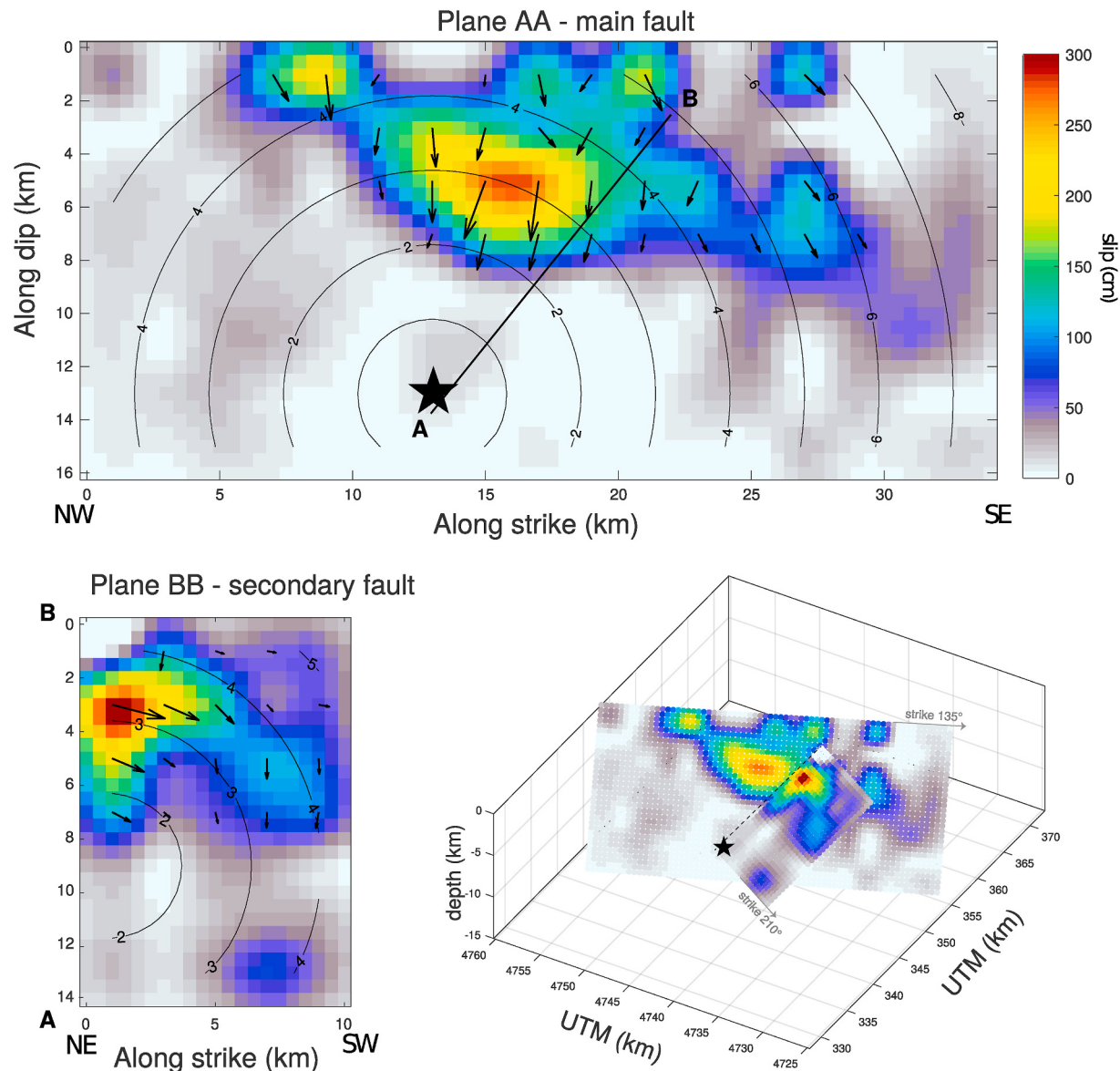


**Fig. 2.** The slip distribution model on the Norcia fault segment proposed by Scognamiglio et al. [1] is used in our hybrid broadband ground-motion simulations. Slip amplitudes are presented in centimeters. The AB black line illustrated on the main fault indicates the intersection with the second fault. The 3-D plot shows and indicates the relative location of the two fault planes.

domain. We used the steady level of acceleration in the Fourier domain consistent with the standard choice being around 0.5–0.8 Hz frequency [28]. The LF component is selected to merge with the HF part. While the vertical components of the two procedures are well oriented, the two horizontal HF components are rotated in increments of one degree to determine the best match with the horizontal components of the LF part of the motion. Before merging, the classic long-term and short-term average automatic selection algorithm is used to synchronize the time of the signals. Therefore, the result of this processing is henceforth referred to as a hybrid broadband seismogram.

In section 5.2, we reported some examples of constructing a hybrid broadband horizontal seismogram based on the sum of filtered deterministic LF and stochastic HF composition.

### 3.1. Low-frequency ground-motion simulations

LF seismograms were obtained from a non-negative, least-squares inversion method with simultaneous smoothing and damping based on Hartzell and Heaton [16] and implemented in Dreger et al. [24]. The

technique allows the simultaneous inversion of seismic waveforms up to 0.5 Hz and geodetic data to retrieve the time history of slip in amplitude and direction on a finite fault plane (or more faults) parameterized in terms of equal-area sub-faults.

This method has been proposed to retrieve the rupture history of the main events of the sequence [1,37,39]. This approach allows the use of multiple “time windows” to account for potential variations in rupture velocity and local rise time. In each time window, the rupture front propagates at constant rupture velocity and the source time function is a boxcar, representing the slip velocity, having a fixed duration (rise time). Multiple “time windows” allow for the possibility that a given sub-fault can rupture multiple times and not necessarily at the first window.

Multiple fault segments are employed to model faults with different strike and dip. The segments’ timing is specified for a starting sub-fault on each segment, which is defined by the delay time concerning the earthquake origin time. The values of slip duration and rupture velocity, as well as the local position of the rupture initiation point on a successive fault plane and its temporal delay are thus selected iteratively by

**Table 2**

Source, Path, and Site parameters used as input for the high-frequency stochastic simulation.

Parameter	Value or function	Reference
Source		
Hypocenter	lat, lon, dep 42.84°, 13.11°, 9.52 km	INGV
Rupture model	strike, dip, sub-faults number Plane AA: 155°, 47°, 354 Plane BB: 210°, 36°, 99	[1]
Rupture time	According to Rupture model	[1]
Magnitude	M6.5, using Plane AA: M6.38, Plane BB: M6.15	[1]
Stress drop	22 MPa	[14,43]
Velocity model	1D regional structure	[38]
Properties at source	$\alpha = 6.01 \text{ km/s}$ , $\beta = 3.43 \text{ km/s}$ , $\rho = 2.70 \text{ gr/cc}$	[38]
<b>Path</b>		
Geometrical spreading	$G(R) = \begin{cases} R^{-1.1} & \text{if } R \leq 10 \text{ km} \\ \left(\frac{1}{10}\right)^{1.1} \left(\frac{R}{10}\right)^{-1.0} & \text{if } 10 < R \leq 30 \text{ km} \\ \left(\frac{1}{10}\right)^{1.1} \left(\frac{30}{10}\right)^{-1.0} \left(\frac{R}{30}\right)^{-0.7} & \text{if } 30 < R \leq 100 \text{ km} \\ \left(\frac{1}{10}\right)^{1.1} \left(\frac{30}{10}\right)^{-1.0} \left(\frac{100}{30}\right)^{-0.7} \left(\frac{R}{100}\right)^{-0.5} & \text{if } R > 100 \text{ km} \end{cases}$	[2]
Quality factor	$Q_S(f) = 140 f^{0.25}$ , $Q_P(f) = 315 f^{0.25}$	[2,23]
<b>Site</b>		
Kappa	$\kappa_{0_A} \in [0.020 - 0.025] \text{ s}$ for site A $\kappa_{0_B} \in [0.030 - 0.035] \text{ s}$ for site B $\kappa_{0_C} \in [0.040 - 0.045] \text{ s}$ for site C	[46]
Amplification	GRSA for all stations SATF for some stations with available $V_S$ profile	[27], [41,42,45]

GRSA: Generic Rock Soil Amplification; SATF: Soil Amplification Transfer Functions.

performing inversions with different values of these parameters and by quantitatively measuring the fit based on a variance reduction, as defined in Ref. [24]. Starting from the best kinematic model (whose details are in section 4.1), we generated the LF waveforms for frequencies up to 1 Hz at all the stations of Table 1 through a forward model. LF waveforms are obtained by convolving the slip rupture history on the faults with the Green's functions computed at the same frequencies by using the 1D velocity model calibrated for Central Italy [38].

### 3.2. High-frequency ground-motion simulations

HF seismograms were obtained employing a stochastic method to simulate P, SV, and SH waves that allow us to obtain horizontal and vertical strong-motion accelerograms. We adopted the methodology proposed by Otarola and Ruiz [23] and Ruiz et al. [25] (see details and references therein) who modeled the Fourier Spectrum of synthetic acceleration ( $A_{ijm}^X$ ) following Eq. (1),

$$A_{ijm}^X = \frac{\mathcal{R}_{ijm}^X F_{ijm}^X EP_{ijm}^X M_{0ij}}{4\pi\rho v^3} \frac{1}{1 + \left(\frac{f}{f_{ij}^X}\right)^2} G(R_{ijm}) \exp\left(-\frac{\pi f R_{ijm}}{Q_X(f) v}\right) Amp(f) \exp(-\pi \kappa_{0m} f) (2\pi f)^2 \quad (1)$$

in which the superscript X corresponds to P, SV or SH waves, the velocity parameter  $v$  could be P or S wave velocity. The subscripts  $i, j$  indicate sub-faults positions and the rupture time in which this sub-fault is activated, finally the subscript  $m$  indicate the station simulated (more details about the temporary evolution is described in Ref. [25]).

The source parameters include free surface factors (FS) and energy partition (EP) obtained by incident and azimuthal angles of direct seismic rays from source to the station; also we include the seismic

moment of each sub-fault ( $M_{0ij}$ ) and the physical parameters around the source vicinity such as density ( $\rho$ ), P- and S-waves velocities. We include a  $\omega^{-2}$  model [40] and dynamic corner frequency ( $f_{cij}$ ) for P or S waves [22,23]. Here, we incorporate the exact values of radiation patterns for P, SV and SH waves ( $\mathcal{R}$ ) of each sub-fault following the formulation of Aki and Richards [26] (Eqs. (2)–(4)),

$$\begin{aligned} \mathcal{R}_{ijm}^P &= \cos(\lambda_{ij}) \sin(\delta_{ij}) \sin^2(i_{eijm}) \sin(2(\varphi_{ijm} - \varphi_{sij})) \\ &\quad - \cos(\lambda_{ij}) \cos(\delta_{ij}) \sin(2i_{eijm}) \cos(\varphi_{ijm} - \varphi_{sij}) \\ &\quad + \sin(\lambda_{ij}) \sin(2\delta_{ij}) [\cos^2(i_{eijm}) - \sin^2(i_{eijm}) \sin^2(\varphi_{ijm} - \varphi_{sij})] \\ &\quad + \sin(\lambda_{ij}) \cos(2\delta_{ij}) \sin(2i_{eijm}) \sin(\varphi_{ijm} - \varphi_{sij}) \end{aligned} \quad (2)$$

$$\begin{aligned} \mathcal{R}_{ijm}^{SV} &= \sin(\lambda_{ij}) \cos(2\delta_{ij}) \cos(2i_{eijm}) \sin(\varphi_{ijm} - \varphi_{sij}) \\ &\quad - \cos(\lambda_{ij}) \cos(\delta_{ij}) \cos(2i_{eijm}) \cos(\varphi_{ijm} - \varphi_{sij}) \\ &\quad + 0.5 \cos(\lambda_{ij}) \sin(\delta_{ij}) \sin(2i_{eijm}) \sin(2(\varphi_{ijm} - \varphi_{sij})) \\ &\quad - 0.5 \sin(\lambda_{ij}) \sin(2\delta_{ij}) \sin(2i_{eijm}) [1 + \sin^2(\varphi_{ijm} - \varphi_{sij})] \end{aligned} \quad (3)$$

$$\begin{aligned} \mathcal{R}_{ijm}^{SH} &= \cos(\lambda_{ij}) \cos(\delta_{ij}) \cos(i_{eijm}) \sin(\varphi_{ijm} - \varphi_{sij}) \\ &\quad + \cos(\lambda_{ij}) \sin(\delta_{ij}) \sin(i_{eijm}) \cos(2(\varphi_{ijm} - \varphi_{sij})) \\ &\quad + \sin(\lambda_{ij}) \cos(2\delta_{ij}) \cos(i_{eijm}) \cos(\varphi_{ijm} - \varphi_{sij}) \\ &\quad - 0.5 \sin(\lambda_{ij}) \sin(2\delta_{ij}) \sin(i_{eijm}) \sin(2(\varphi_{ijm} - \varphi_{sij})) \end{aligned} \quad (4)$$

in which  $\lambda$ ,  $\delta$ ,  $\varphi_S$  are rake, dip and strike of the fault plane, respectively, and  $i_e$ ,  $\varphi$ , are the take-off angle and source-receiver azimuth, respectively. Following the same notation than Eq. (1), the subscripts  $i, j$  indicate sub-faults positions and rupture time, and the subscript  $m$  indicate the station simulated.

Regarding the path parameters presented in Eq. (1), we incorporate both geometrical spreading ( $G(R)$ ) and anelastic attenuation by using quality factors ( $Q(f)$ ). Finally, the site parameters includes a high-frequency attenuation using kappa filter ( $\kappa_0$ ) and soil amplification ( $Amp(f)$ ). The stations simulated are located over different soil deposits characterized by their  $V_{S30}$  information. Then, to better address the soil

amplification factors we used the generic rock soil amplification (GRSA) by using the soil classification of the NTC-18 code [27]. Besides, if we have the information of the local velocity structure, from the surface to hard rock, below each station, we estimate the soil amplification transfer functions (SATF) associated with each type of wave following the descriptions given by Kausel and Roësset [41] and Kausel [42] and implemented in Ruiz et al. [25].

#### 4. Input parameters to generate broadband seismograms

In this section, we described the finite fault source model used to build LF and HF seismograms and some regional and local parameters introduced in the stochastic strong-motion simulation adopted in our study.

##### 4.1. Finite-fault source model

The finite fault rupture history of the Norcia earthquake has been investigated by jointly inverting the geodetic and seismic datasets by Scognamiglio et al. [1]. This kinematic model, adopted in this study, presents a complex rupture geometry composed of the two fault segments: the main fault N155° striking, SW dipping fault, and a secondary fault plane striking N210° and dipping 36° to the NW. The hypocenter (42.84°N, 13.11°E, 9.52 km depth) belongs to the main fault and intersects the secondary fault in the bottom left corner (see Fig. 2). The main fault is 34 km long and 16 km wide (downdip), while the secondary fault is 10 km long and 14 km wide. Co-seismic slip is concentrated in two prominent patches located on both fault segments reaching a maximum slip of  $\sim 3$  m. The main fault is characterized by a normal mechanism, while the secondary fault by a predominantly strike-slip faulting mechanism. The total inferred seismic moment is  $8.8 \times 10^{18}$  Nm (M6.56), distributed into  $5.9 \times 10^{18}$  Nm (M6.45) on the main fault and  $2.9 \times 10^{18}$  Nm (M6.25) on the secondary fault. The largest asperity is located on the main fault along dip  $\sim 8$  km above the hypocentre at a depth of  $\sim 4.5$  km, with an average mean slip of 2.8 m. The rupture velocity of each time window is 2.7 km/s for the main fault 2.8 km/s for the secondary fault, and the rise time is 1.2 s. The velocity and rise time variability are allowed by using three time windows delayed by the rise time duration. The main fault is characterized by a predominantly normal mechanism while the secondary fault by a predominantly left-lateral strike-slip.

In Fig. 2 two fault segments are presented: the main fault is indicated with "Plane AA" and the secondary fault is indicated with "Plane BB". In the same figure, the 3D plot shows the relative location of the two fault planes. The originally modeled fault planes were parameterized using sub-faults with a  $2 \times 2$  km<sup>2</sup> area to retrieve the slip distribution frequencies up to 0.5 Hz. To include the finite fault source contribution in both LF and HF waveforms the original slip distribution is interpolated, and both fault planes used for our simulations are discretized into 354 (main fault) and 99 (secondary fault) sub-faults, each sub-faults having a  $0.5 \times 0.5$  km<sup>2</sup> area along strike and dip. From the slip distribution we retrieved the variable seismic moments  $M_{0y}$  and the dynamic corner frequencies of each sub-fault to be used in Eq. (1).

Finally, we adopted a value of 22 MPa for the stress drop ( $\Delta\sigma$ ) to calibrate the high-frequency spectral amplitudes (Table 2) following the previous simulations generated in the same region by Ugurhan et al. [43] for the 2009, 6th April L'Aquila earthquake and by Pischiutta et al. [14] for the 2016, 24th August Amatrice earthquake.

##### 4.2. High-frequency seismic wave attenuation model

Seismic attenuation in stochastic simulation is a fundamental physical parameter that presents an essential role in controlling both the shape and the spectra' amplitude. In this study, we used a well-resolved region-specific attenuation model proposed by Malagnini et al. [2]. This model provides a complete description of the source's characteristics

and the attenuation of the ground-motion in the Central Apennines. The attenuation model is constructed using a large set of broadband data of the mainshock and aftershocks of the April 16, 2009 M6.3 L'Aquila seismic sequence. The crustal seismic attenuation, quantified by the quality factor  $Q$  is obtained,  $Q(f) = 140 f^{0.25}$  together with the geometrical spreading coefficient,  $G(R)$ , defined as bilinear relationships. For distances up to 40 km, based on a spherical earth model with a 30 km thick crust, it presents a body-wave-like function as  $G(R) \propto R^{-1.1}$ , and for distances beyond 30 km and 100 km, it changes to a functional form  $G(R) \propto R^{-0.7}$  and  $G(R) \propto R^{-0.5}$  expected for surface waves. The physical parameters that characterize the earthquake source rupture and the seismic wave propagation are listed in Table 2.

#### 4.3. Site amplifications

Site amplification is one of the crucial parameters that contribute to ground-motion, controlling damage in urban areas from large earthquakes. Many studies have demonstrated that the amplitude and frequency content of the ground-motion are mostly affected by the surface geology and soil conditions. We adopted theoretical amplification factors and the GRSA curves [27]. We favored three amplification curves representative of the different site classes defined in the Italian seismic design code NTC-18 (A, B, and C) based on the average shear-wave velocity of the subsoil in their first 30 m, given by the  $V_{S30}$  parameter, as proposed in Pischiutta et al. [14]. In order to model the spectral decay at high frequencies, we used different values for the different site classes (Table 2) for the parameter  $\kappa_0$ , which is a diminution operator accounting for de-amplification effects from the near-surface as defined in Anderson and Hough [44]. The above-described values for  $V_{S30}$  and  $\kappa_0$  were adopted in stochastic simulations for the 98 strong-ground-motion sites, according to each station site class (some given in Table 1). To account for the proper ground-motion amplifications on the vertical component, we have advised the site amplification factors determined from the horizontal-vertical spectral ratios (HVS) by Felicetta et al. [45]. In this recent study, the amplification factors were defined to quantify the site effects in ground-motion amplification in the area where the central Italy seismic sequence occurred. They observed that the amplifications vary as a function of periods between 0.1 s and 1.1 s, being almost 0.74 times larger in the horizontal component than the vertical one.

We point out that the adopted GRSA, calculated through the quarter wavelength approach (hereafter, QWL method) [27,46] using the averaged velocity over the uppermost 30 m of the soil, are characterized by velocity gradients. Neglecting the distinct geological characteristics of the soil layers they are not sensitive to impedance contrasts between the layers [47,48]. So, the GRSA might not be able to adequately quantify the realistic site transfer function being the fundamental resonant peaks generated by the presence of the strong bedrock/soil seismic impedance contrasts. To investigate this effect, we calculate the SATF [41,42] for some stations depending on the local soil velocity profile together with the incident angle for P, SV, and SH waves. In this study, we estimated the SATF given by Ruiz et al. [25], considering that the deeper layer of the velocity profile (>30 m) is near hard rock ( $V_S > 1500$  m/s). Since the shear velocity profiles are available only for a few station's site, we adopted five well-defined velocity profiles corresponding to three different site classification (A, B, and C-D), MMP1, CTD, BRS, GSA, and BTT2 available in the ITACA database to calculate SATF where we considered thickness of each layer and P-, S- waves velocities (see section 5.2 for details).

## 5. Results

### 5.1. Complex fault rupture and secondary fault effect

Here, we investigate the complex fault rupture of the Norcia earthquake and its effect on the ground-motion simulations. To do so, first, we

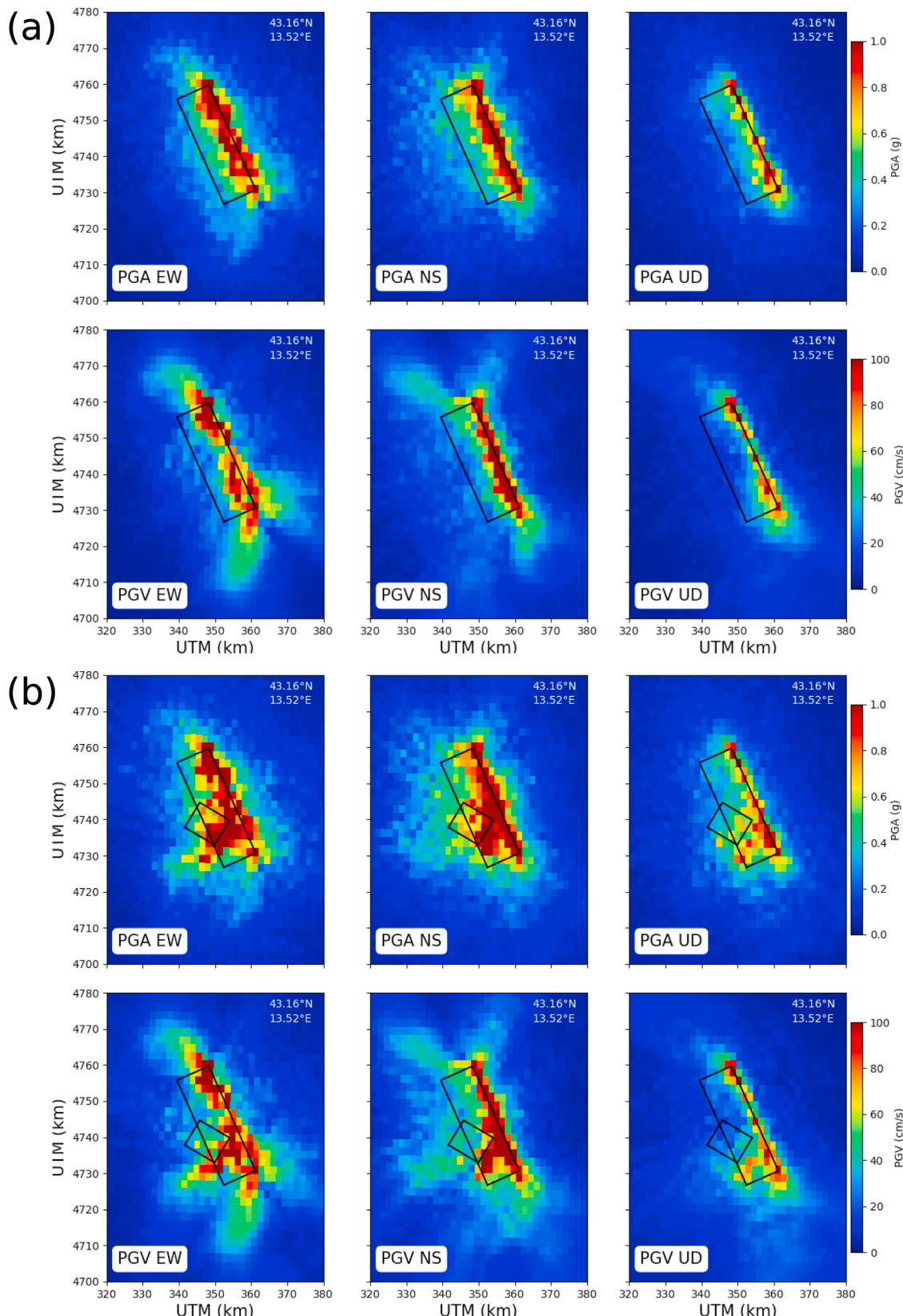


**Fig. 3.** Spatial distributions of simulated ground-motion (for three-components) are determined using the parameters given in Table 2 and for the B site class in terms of peak ground acceleration (PGA, g) values and peak ground velocity (PGV, cm/s) values for Norcia M6.5 earthquake. The region is divided into regular grid spacing of  $2 \times 2 \text{ km}^2$ , such that the simulations are performed for the 2600 virtual stations; (a) the PGA (upper panel) and PGV (lower panel) maps for two horizontal EW, NS, and vertical UD components considering only the contribution of the main rupture (Plane AA) (b) The same as (a) considering the contribution of both the fault planes (Plane AA+BB).

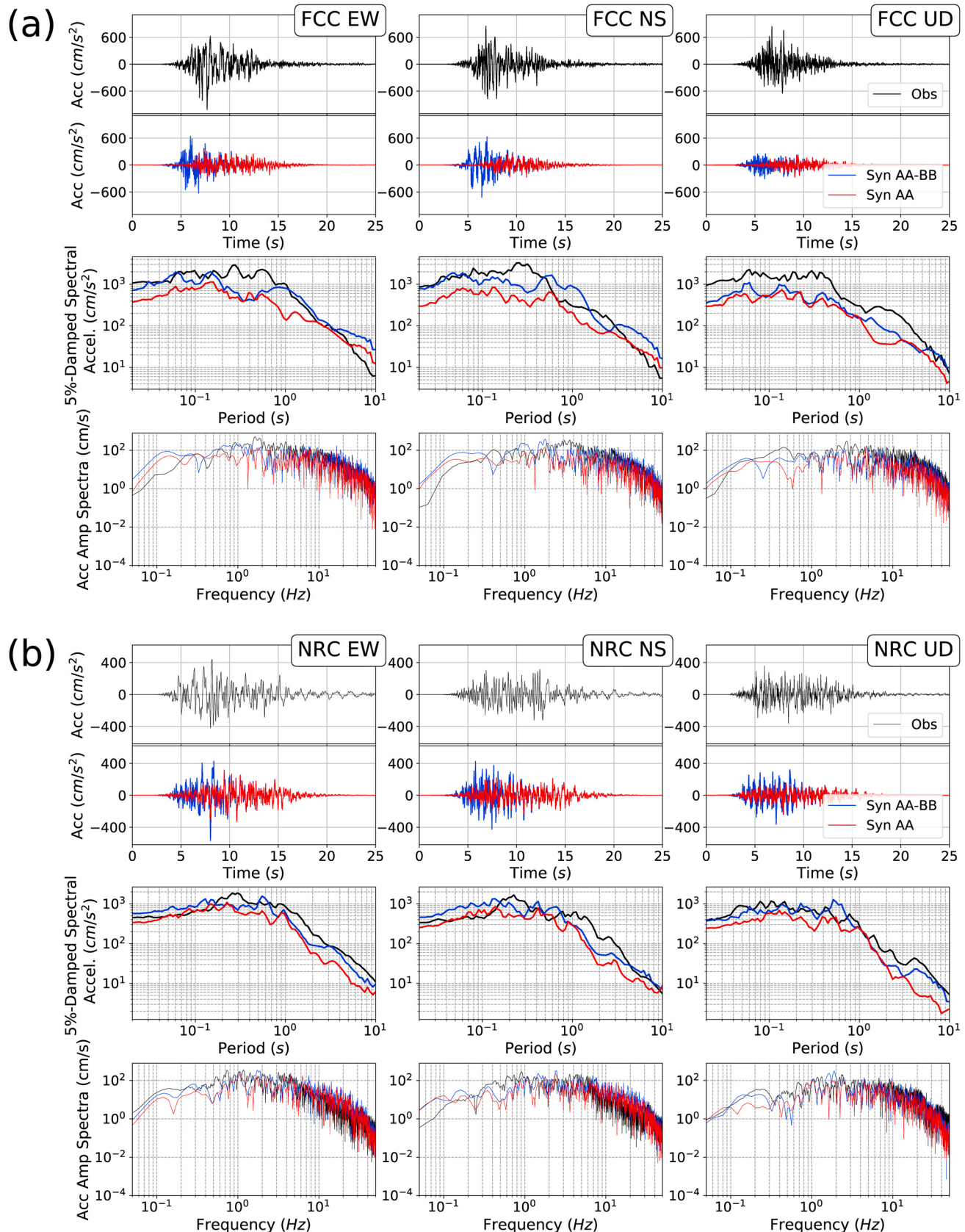


**Fig. 4.** Investigation of the secondary fault effects on HF ground-motion simulations. Comparison of simulated time histories, PSAs (5% damped), and the FAS calculated considering (1) a single fault rupture, Plane AA and (2) two rupture segments, Plane AA+BB with recordings at two closest stations, (a) FCC and (b) NRC to two fault segments.

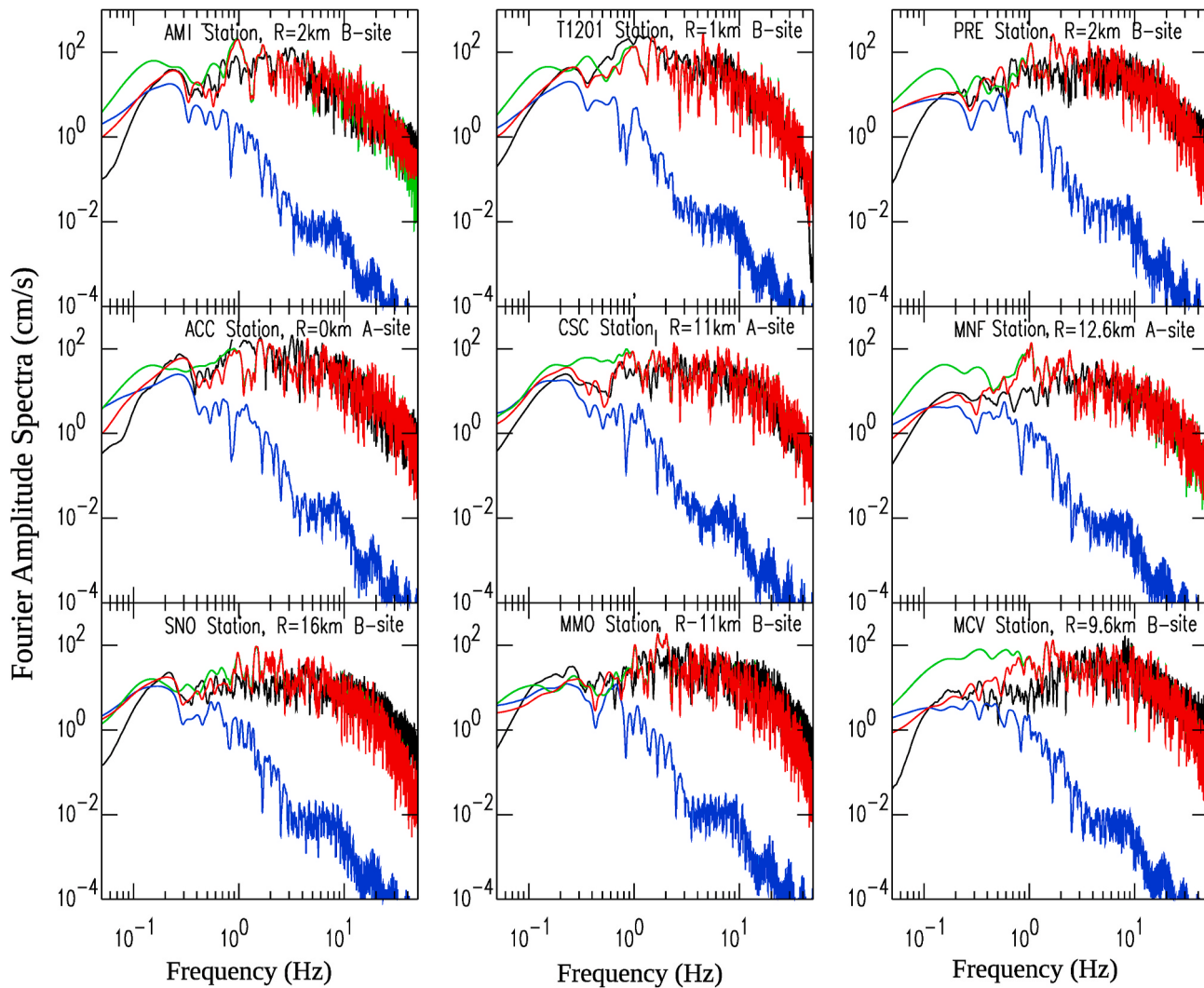


**Fig. 5.** Example of low-frequency (blue) and high-frequency (green) NS horizontal-component acceleration synthetic's FAS at nine stations. Both spectra are combined using a complementary filter around 0.5–0.8 Hz after a time synchronization. The resulting FAS are given with red-colored curves and compared with the observed waveforms (black) for NS components. (For interpretation of the references to color in this figure legend, the reader is referred to the Web version of this article.)

considered only a single fault plane (called Plane AA), which was the main rupture, and then we used both faults together as Plane AA + Plane BB (that is the secondary fault plane), as shown in Fig. 2 to build the ground-motion simulation.

To investigate the spatial ground-motion variability caused by the fault complex rupture processes, mechanism, and the heterogeneous slip distribution over the main and secondary fault, we selected a region between  $12.6^\circ - 13.6^\circ$  E and  $42.3^\circ - 43.3^\circ$  N. We generated the three-components high-frequency time histories at 2600 virtual stations discretizing the selected region into  $2 \times 2 \text{ km}^2$  sized grids and at two near-fault stations (FCC and NRC) considering only the contribution of the main rupture (Plane AA) or both the fault planes (Plane AA+BB). We adopted a uniform site amplification for the virtual stations, testing both A and B site classes. In Fig. 3a, we presented the spatial distribution of the PGA and PGV values at three-components obtained from the simulations using only the main fault rupture within the selected area in case of the B site classification, while the effect of the complex rupture, considering two ruptured segments, over the PGA and PGV ground-motion parameters are given in Fig. 3b respectively. Results obtained using the A site class for both rupture models are presented in Fig. S1a and Fig. S1b in the supplementary electronic material.

Since an invariant soil condition is utilized in our simulations, the

ground-motion parameters' spatial distributions predominantly mimic the source effect. The PGA and PGV distributions in Fig. 3b present the largest ground shaking observed along the fault rupture and particularly around the large slip asperity area close to the surface rupture fault zone. The largest PGA and PGV values of  $1008 \text{ cm/s}^2$  and  $69 \text{ cm/s}$ , respectively, both observed in FCC station (see Table 1) agree with those obtained with the spatial distribution high-frequency simulations, in which we recover PGA values of the order of  $980 \text{ cm/s}^2$  and PGV values greater than  $90 \text{ cm/s}$  in the near-source region. Moreover, we observed the spatial apparent radiation patterns characterized by normal faulting mechanisms on the ground-motion parameters in PGA and PGV. The seismic waves' radiation effect and its spatial variation obtained from the two segmented models are distinct and noticeable in areas close to the fault rupture and different respect obtained from the main fault. Our stochastic simulations at high frequencies mimic the source rupture complexity including the faulting mechanism, slip distribution, stress drop as well as the radiation pattern to the near source area while the source related directivity effect is guaranteed by the low-frequency part of the simulations.

HF simulated time histories are calculated at near-fault stations, FCC, and NRC located on the fault plane, with Joyner and Boore distance ( $R_{jb}$ ) of 0 km and 1.21 km, respectively. As site amplification, we considered

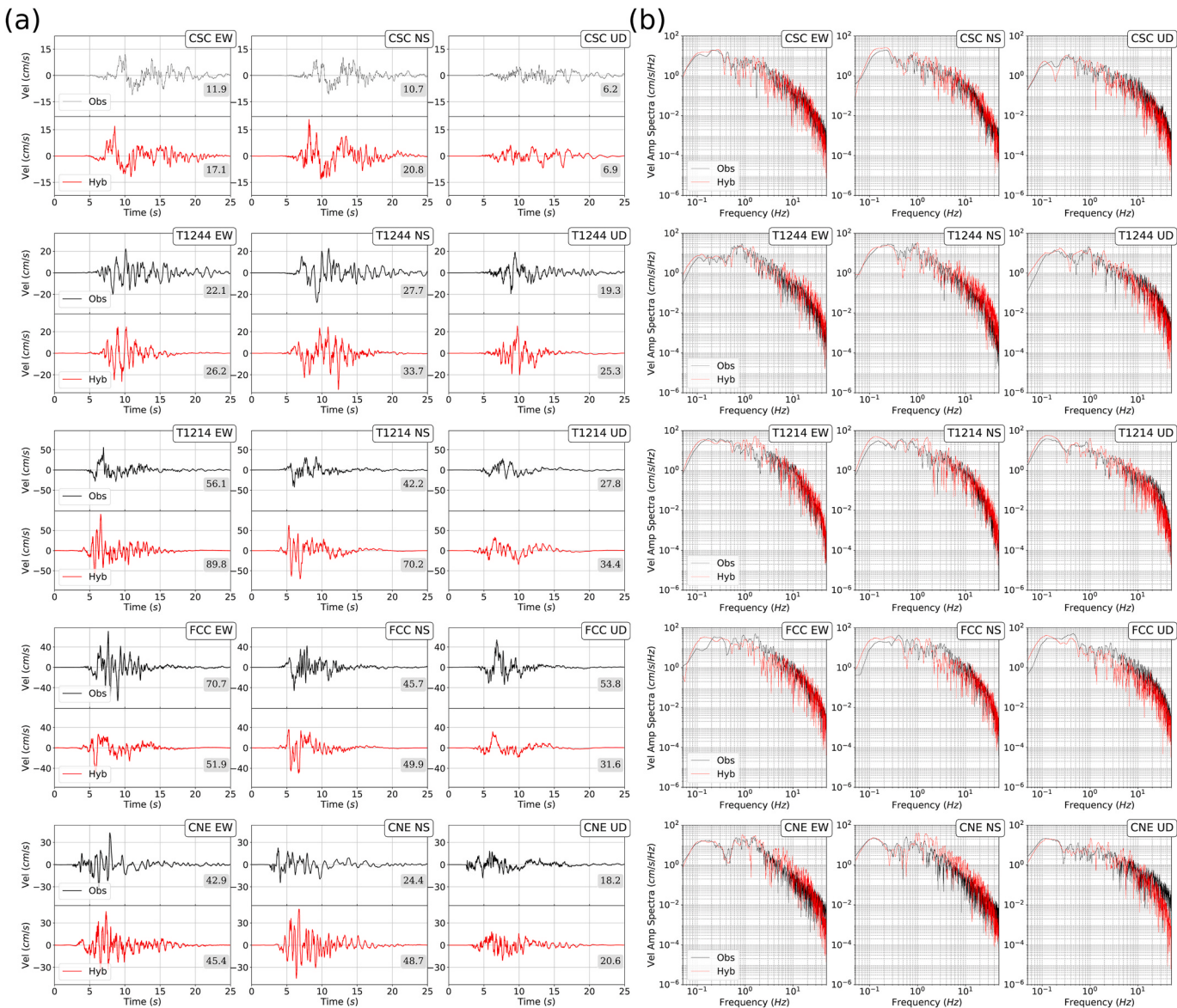


**Fig. 6.** Comparison of the real (black) and simulated (red) (a) velocity waveforms (cm/s) and (b) FAS for EW, NS, and UD components at five stations (CSC, T1244, T1214, FCC, and CNE). Numbers in the left panel indicate the peak ground velocity, PGV values for each waveform. (For interpretation of the references to color in this figure legend, the reader is referred to the Web version of this article.)

the GRSA as corresponding to the A and B type site classifications for FCC and NRC stations, as indicated in the ITACA database, respectively. In Fig. 4a and b, we compared simulated time histories, Pseudo-spectral acceleration (PSA, 5% damped), and the Fourier amplitude spectra (FAS), calculated considering: (1) a single rupture and (2) two rupture segments, with recordings at two closest stations to the two fault segments. We observed that the HF synthetics were improved and fit better to the recorded data in the complex model of fault structure and ground-motion parameters. At station FCC (Fig. 4a), the simulated horizontal average PGA is 301 cm/s<sup>2</sup> from the main fault rupture model (Plane AA) and it is 681 cm/s<sup>2</sup> from the Plane AA+BB that is in good agreement with the observed value 980 cm/s<sup>2</sup>. This improvement is mainly observed at stations close to the epicenter, such as NRC (Fig. 4b).

### 5.2. Broadband simulations versus recordings: time histories and fourier spectra

The BB simulations of the 2016 Norcia earthquake are performed at 98 stations within 100 km  $R_{jb}$  distance. In Fig. 5, FAS at nine selected

stations are related to the BB synthetic signals (red) combining the HF stochastic simulations (green) with the LF simulated seismograms (blue). Recorded data are also reported (black) in the same figure. The final broadbands benefit the regional spectral parameters over larger frequency bands (0.05 – 20 Hz), such as the frequency-dependent seismic quality factor, geometrical spreading coefficient, and the depletion of high-frequency motion at the site, which may be caused by the local  $Q(z)$  structure, as well as the earthquake source complexity. In Fig. 6, the observed and simulated BB ground-motion records are presented for the EW and NS components in terms of the velocity-time histories and FAS at some selected stations. The stations FCC (A site), CNE (B site), and T1214 (B site) are located on the fault rupture plane. Although the station FCC is located on the A site class, the observed averaged horizontal PGA and PGV values, around 930 cm/s<sup>2</sup> - 58.2 cm/s are the larger than those registered at stations CNE, 368 cm/s<sup>2</sup> - 33.6 cm/s and T1214, 548 cm/s<sup>2</sup> - 49.2 cm/s at B site class, respectively. This large acceleration at station FCC may be caused by the high-slip rupture patches in the two fault planes and the rupture directivity effect on the fault plane's hanging wall sector. The simulated ground-motions in

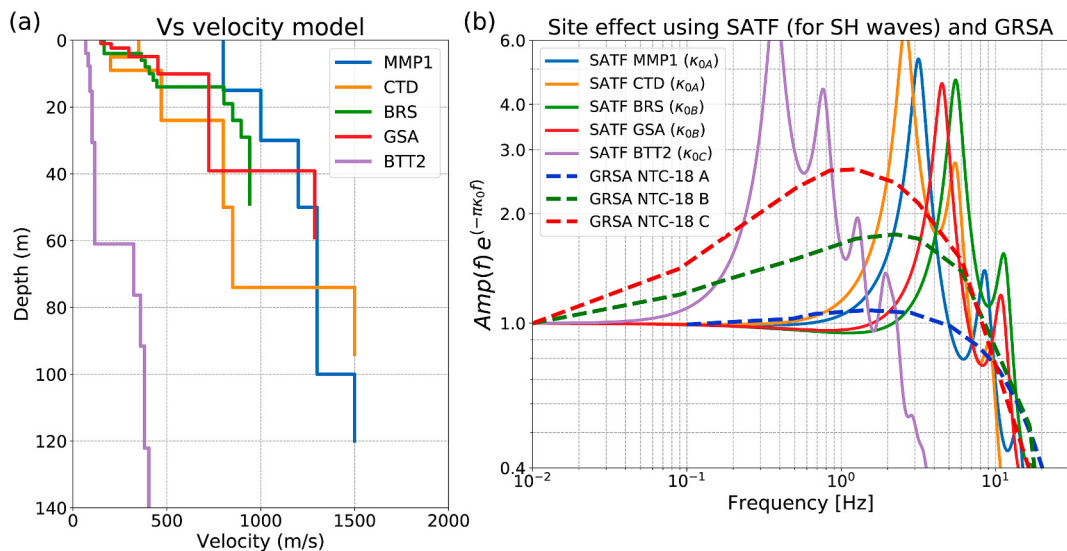


**Fig. 7.** (a) The velocity profiles at stations MMP1, CTD (NTC-18 A site class), BRS, GSA (NTC-18 B site class), and BTT2 (NTC-18 C-D site class) adopted from the ITACA database. (b) Site effects using SATF and GRSA. Continuous curves correspond to the site amplification of the SH wave in stations MMP1, CTD, BRS, GSA, and BTT2. Dashed curves correspond to the generic rock soil amplification (GRSA) for soils A, B, and C. GRSA was calculated using the QWL method.

terms of averaged horizontal PGA - PGV for these sites (FCC, CNE, T1214) are  $678.0 \text{ cm/s}^2$  -  $50.9 \text{ cm/s}$ ,  $803.6 \text{ cm/s}^2$  -  $47.0 \text{ cm/s}$ , and  $945.8 \text{ cm/s}^2$  -  $79.9 \text{ cm/s}$ , respectively.

Station T1244 (A site class) is one the closest stations to the fault rupture ( $R_{jb} = 1.8 \text{ km}$ ). We simulated PGA of  $438.6 \text{ cm/s}^2$  (EW),  $356.8 \text{ cm/s}^2$  (NS) and PGV of  $26.2 \text{ cm/s}$  (EW) and  $33.7 \text{ cm/s}$  (NS), while observed values are  $278 \text{ cm/s}^2$  (EW),  $188 \text{ cm/s}^2$  (NS), and  $21.6 \text{ cm/s}$  (EW),  $27.1 \text{ cm/s}$  (NS), respectively for the two horizontal components. Simulations at CIT (B site class) at  $R_{jb} = 5.8 \text{ km}$  resulted in PGA of  $193.8 \text{ cm/s}^2$  (EW),  $145.3 \text{ cm/s}^2$  (NS), while observed, ranged from  $333 \text{ cm/s}^2$  (EW),  $212 \text{ cm/s}^2$  (NS); simulated PGV was  $18.8 \text{ cm/s}$  (EW),  $9.7 \text{ cm/s}$  (NS), while observed, ranging from  $16.5 \text{ cm/s}$  (EW),  $14.3 \text{ cm/s}$  (NS). The simulated time histories and FAS in both the EW and NS directions at the closest stations closely match the corresponding recorded results. The FAS amplitudes give a good match for the entire frequency range. In Fig. S2 we provide more BB simulations of the 2016 Norcia earthquake as the velocity-time histories that are performed at other 15 stations and their corresponding FAS.

Fig. 7a shows the S-wave velocity profiles of MMP1, CTD, BRS, GSA, and BTT2 stations and Fig. 7b shows their soil amplification curves and their SH SATF. The soil amplification transfer functions for P, SV, and SH waves together with the GRSA of each selected station are plotted in Fig. S3. We can see from the transfer functions that their peaks are very narrow that correspond to response frequency, compared to the generic soil amplification. This information is fundamental and needed to correctly reproduce the soil amplification through the SATF. Fig. 8 shows the synthetic MMP1, CTD, BRS, GSA, and BTT2 strong motion records with those calculated using both the GRSA and SATF. In general, the spectral accelerations are improved by SATF with respect to those determined by GRSA. However, in some cases, clear spectral peaks in the observed records were not reproduced by simulations. For example, the peak amplitude of the NS component of the BRS station and the two horizontal components of the BTT2 station are underestimated by SATF while the resonance frequencies were satisfactorily revealed. Also in other cases, the spectral accelerations are overestimated by SATF with sharp peaks; such as the MMP1 station and the vertical components of CTD and GSA stations where GRSA worked better. A possible explanation for this discrepancy is that most stations do not reach the hard rock value ( $V_s > 1500 \text{ m/s}$ ) not reproducing resonant frequencies correctly. Similar results were obtained for Mw 9.0 Tohoku-Oki, Japan

earthquake, where only the stations with soil profile with boreholes depth at  $V_s > 1500 \text{ m/s}$  were well simulated using SATF [25] on the contrary, using the amplification factors, the surface stations were well modeled [49]. In view of these results for the Norcia earthquake, we suggest modeling the HF strong-motion considering soil amplification curves.

### 5.3. Broadband simulations versus ground-motion empirical equations (GMPEs)

As a further step, we compared the PGA and PGV values of the simulated ground-motions against one local ground-motion prediction equation (GMPE) ([50], hereafter, ITA10) as derived from the normal-faulting style and for three different site classifications. For comparisons, a total of 98 stations are selected. In the simulations at these selected stations, we employ the amplification factors by Pischiutta et al. [14] for different site classes for the high-frequency simulations. The GMPEs are plotted for M6.5, normal-faulting style for three site conditions related to NTC-18 classes-A, -B, and -C, respectively. Fig. 9a and 9b shows the comparisons in terms of PGA and PGV values for different NTC-18 soil classification and the observed data as two horizontal and one vertical components, which indicate a good match with the simulated peaks remaining within  $\pm 1$  standard deviation of the ITA10 GMPEs. Vertical components of the simulations perfectly fit the observed values in both PGAs and PGVs as presented in Fig. 10b with the goodness of fit (GOF [7]) measurement (see details in section 5.4). In general, the generic soil site factors adopted for the simulations were able to reproduce and mimic the observed data's features.

### 5.4. Investigating the model bias and standard error

In this study, to quantify the match between observed and simulated (both HF and BB) results, the frequency/period-dependent GOF are calculated as follows:

$$B(T_k)^Y = \frac{1}{N} \sum_{m=1}^N \left\{ r_m(T_k)^Y = \ln \left( \frac{O_m^Y(T_k)}{S_m^Y(T_k)} \right) \right\} \quad (5)$$

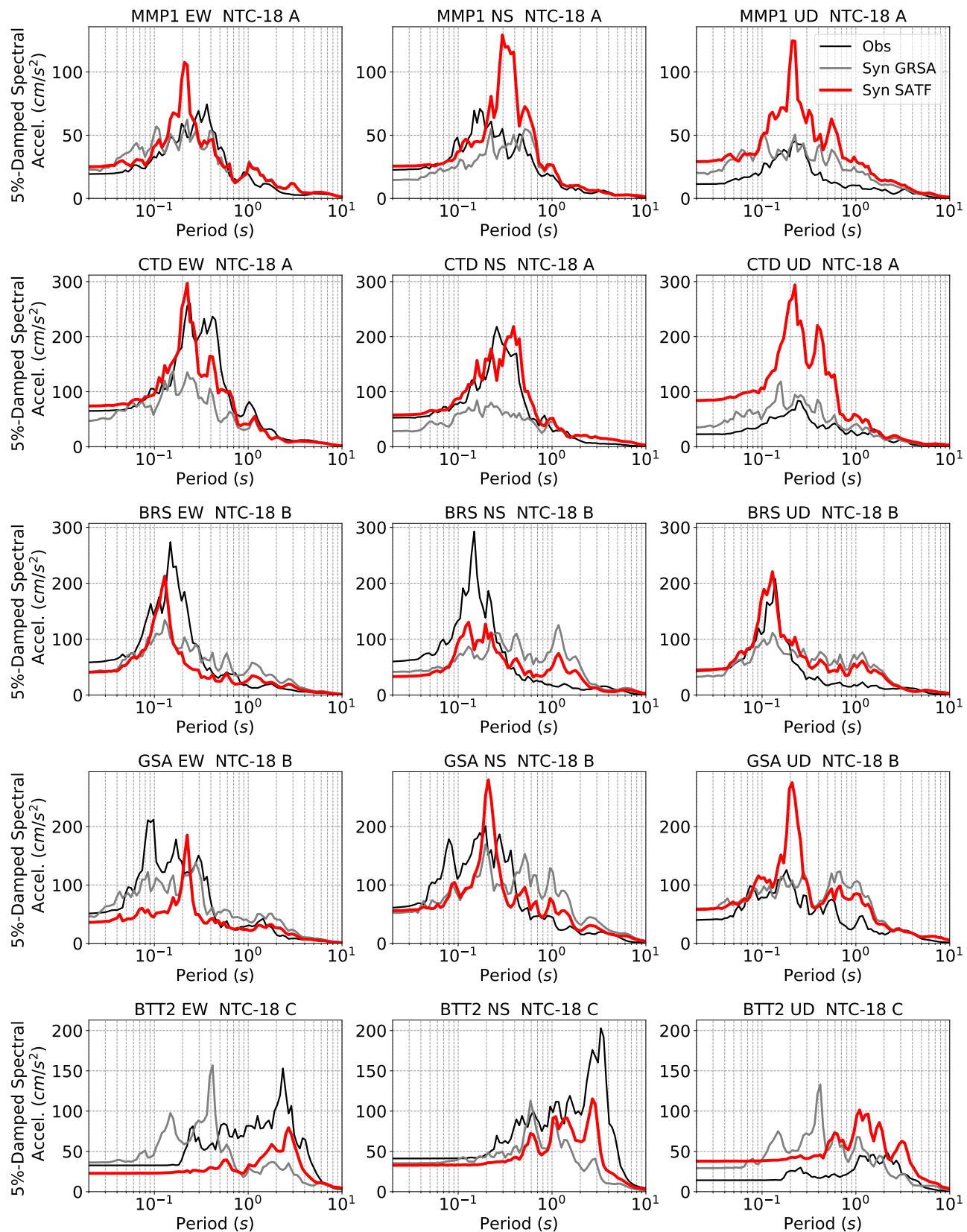


**Fig. 8.** 5% - Damped PSAs for stations MMP1, CTD, BRS, GSA, and BTT2 in their three-components. Black lines correspond to the recorded data, gray lines correspond to the high-frequency simulation using GRSA, and red lines represent the high-frequency simulation using SATF. (For interpretation of the references to color in this figure legend, the reader is referred to the Web version of this article.)

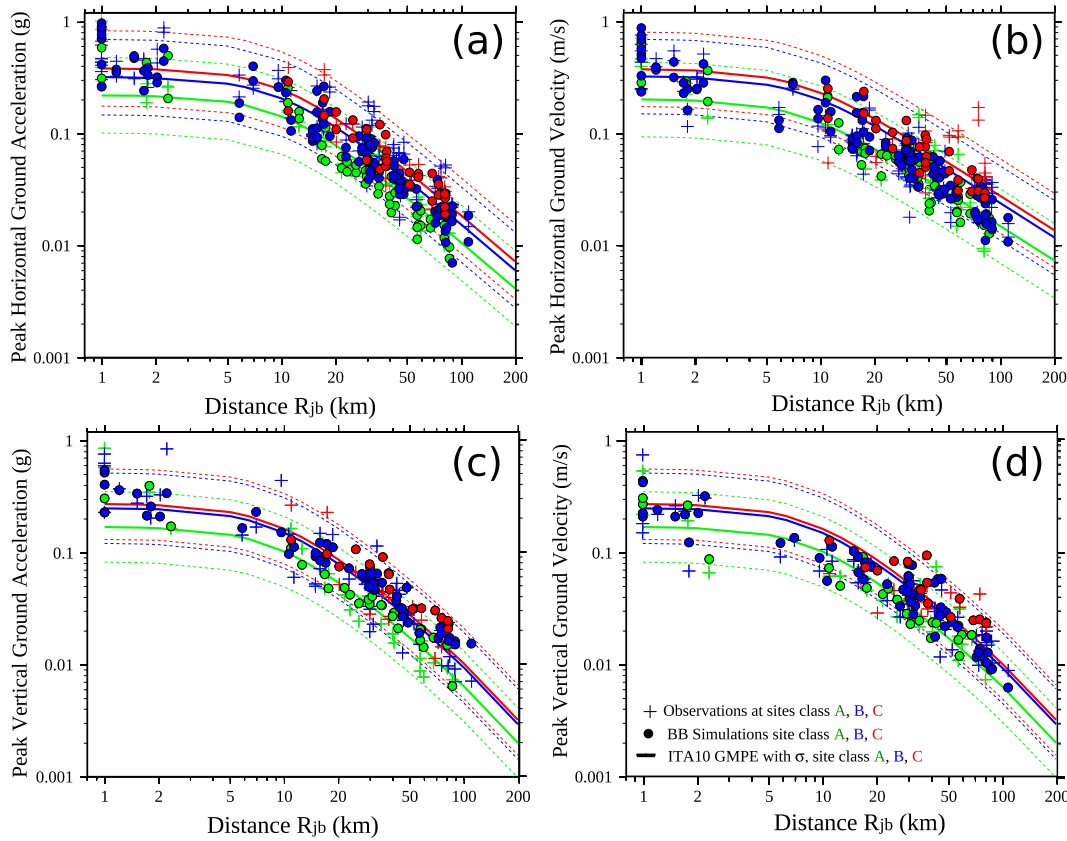


**Fig. 9.** Comparison of observed (a) peak horizontal ground acceleration (g), (b) peak horizontal ground velocity (m/s) (c) peak vertical ground acceleration (g), and (d) peak vertical ground velocity (m/s) values (cross symbol) of the Norcia earthquake M6.5 against the simulated ground-motion parameters calculated at those corresponding stations at site A (green dots), B (blue dots), and C (red dots) classifications and the ground-motion prediction model for Italy, ITA10 as derived by Bindi et al. [50]. (For interpretation of the references to color in this figure legend, the reader is referred to the Web version of this article.)

$$\sigma(T_k)^Y = \sqrt{\frac{1}{N} \left( \sum_{m=1}^N [r_m(T_k)^Y - B(T_k)^Y]^2 \right)} \quad (6)$$

in which  $B(T_k)^Y$  is the model bias depending on  $r_m^Y(T_k)$  the observed spectral acceleration in the station  $m$ , and  $S_m^Y(T_k)$  simulated spectral acceleration. We also calculated the standard deviation  $\sigma(T_k)^Y$ , in which  $T_k$  is the period  $k$ ,  $N$  is the total number of stations and  $Y$  can be the EW, NS, or UD component.

The measure of goodness of fit summarizes the difference between the observed value and the expected value under our model, which predicts ground shaking and helps describe how well the simulation fits a set of observations. A perfect fit would result in zero  $B(T_k)$  in Eq. (5). In general values of  $B(T_k)$  included between  $-1.5$  and  $1.5$  are considered as successful modeling, as well as low standard deviation values, Eq. (6) [7].

Fig. 10a, b, and 10c show the goodness of fit between observed and simulated PSAs of 5% damping both for HF and BB for a total of 98 stations registered during M6.5 Norcia earthquake within a distance of 100 km. Long periods are underestimated by the stochastic methodology HF only; this is clear in the GOF (see Fig. 10a) while the BB simulations successfully produce the observed ground-motions also for longer periods ( $>1$  s) (see Fig. 10b). We obtain standard deviation values lower than 1.0 natural log units for the three-components in our simulation, which reflects a well-performed modeling. In Fig. 10c, we also presented the residuals between observed and simulated ground-motion parameters, PGA, and PGV for the three-components of all ninety-eight stations. Model bias is calculated for each component of BB simulations averaging over the sites, the natural logarithm of the ratio of the observed to the simulated in terms of PGA and PGV parameters. The standard deviation

for PGA parameters derived from the residuals between BB simulations and observed data following Eq. (5) and (6), and obtained as 0.22, 0.18, and 0.24 for each component, EW, NS, and UD, respectively. In the case of the PGV, they are 0.23, 0.22, and 0.17 for EW, NS, and UD components, respectively.

## 6. Conclusive remarks

The main results and conclusions derived in this study are given as follows:

1. We simulated BB synthetics based on a proposed hybrid technique for the Central Italy M6.5 Norcia earthquake. Synthetic seismograms were produced at stations where the observations were recorded for distances to the fault up to 100 km. The new HF method allows us to generate the three-components (EW, NS, UD) instead of obtaining only one generic horizontal component. Therefore in this work, it has been possible to merge the HF with the LF data and perform BB simulations separately for each orthogonal component.
2. The complex fault rupture of the Norcia earthquake is successfully used to generate BB synthetic waveforms. Including both the fault planes instead of using only the main fault (Plane BB and Plane AA) improves the fit to recorded ground-motions and time histories, particularly in the near-source area.
3. We propose to use the method of Soil Amplification Transfer functions only when we have information on the velocity profiles of the soil to the hard rock ( $V_S > 1500$  m/s). In cases where only  $V_{S_{30}}$  information is available, we recommended using Generic Rock Soil Amplification factors.

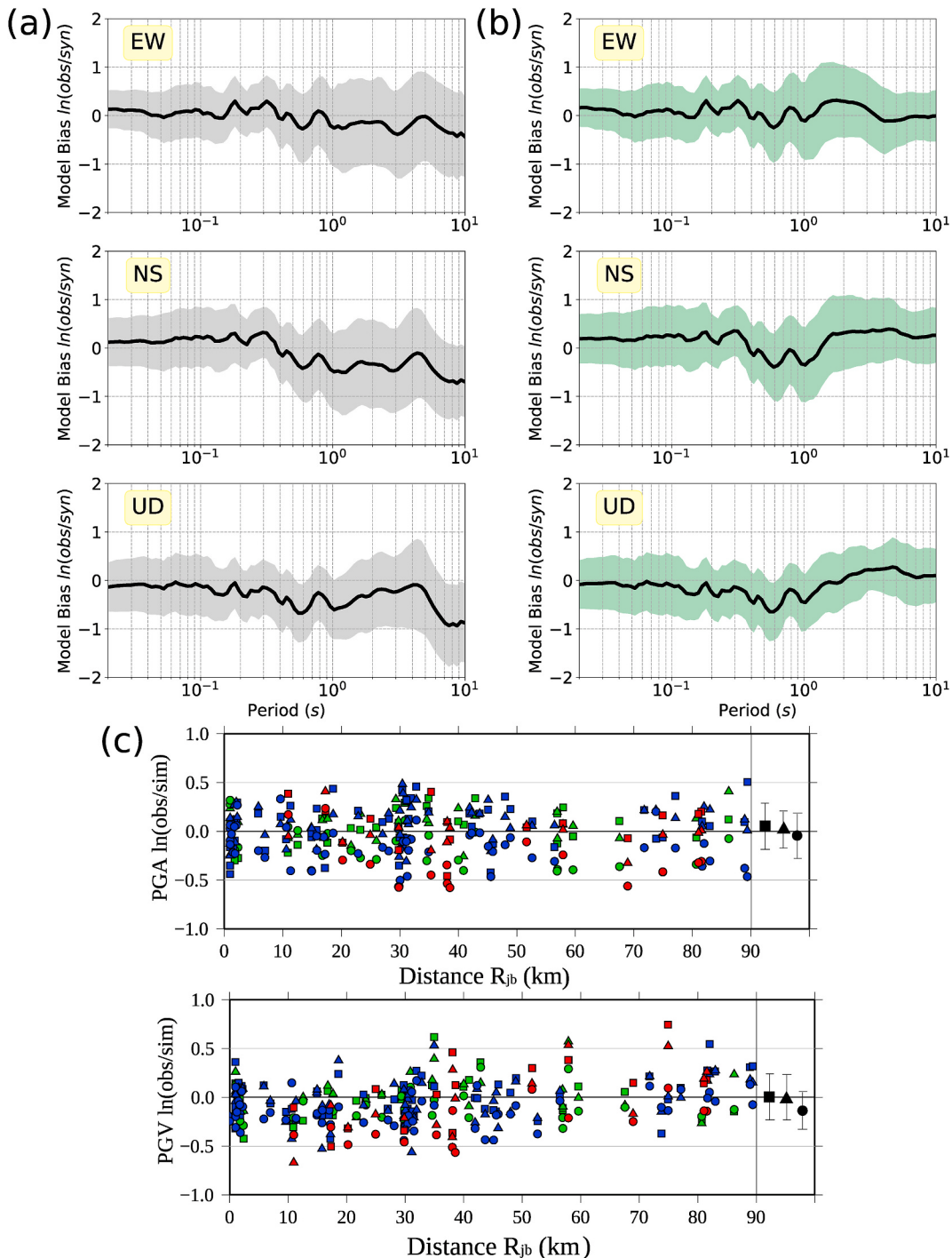


**Fig. 10.** Horizontal and vertical spectral acceleration goodness of fit for the Norcia M6.5 earthquake simulations averaged over 98 stations. The residuals used to determine the goodness of fit are computed between the simulations determined with (a) the high-frequency (left column) as well as (b) the hybrid method (right column) and the recorded data; (c) Residuals calculated between the simulated PGA and PGV values for three-components, EW (square symbol), NS (triangle symbol), and UD (circle symbol). Symbol colors present the different site classification; A-site (green), B-site (blue) and C-site (red) according to NTC-18 on the basis of the  $V_{S30}$  parameter, plotted as functions of Joyner and Boore distance. (For interpretation of the references to color in this figure legend, the reader is referred to the Web version of this article.)

4. The simulated motions at the selected stations are compared against the observed records through ground-motion misfits. The simulated PGA and PGV values are then compared against the Italian GMPEs [50]. The close match between the simulated peak values and the corresponding values obtained from the GMPEs indicates physically reasonable and reliable source, propagation, and site modeling despite the existing uncertainties in the region.

5. PSAs of the BB synthetics with 5% damping together with the PGA were compared with the observed time histories and the ground-motion parameters GMPEs proposed by Bindi et al. [50]. Our results show that an overall agreement between the synthetics PSAs and attenuation relations has been observed.
6. In this study, we demonstrated the importance of choosing the critical region-specific source and attenuation parameters and their

influence (particularly source and site-related parameters) on the simulated ground-motions.

## Declaration of competing interest

The authors declare that they have no known competing financial interests or personal relationships that could have appeared to influence the work reported in this paper.

## Acknowledgments

The study was partially funded by the Italian Presidenza del Consiglio dei Ministri - Dipartimento della Protezione Civile (DPC) - Agreement B1, DPC-INGV 2019–2021. This paper does not necessarily represent DPC official opinions and policies. During this work at the INGV in Rome, Italy, Javier Ojeda from the Universidad de Chile, Departamento de Geofísica, Santiago, Chile was supported by the Centro per la Pericolosità Sismica (CPS) of INGV. SR thanks Agencia Nacional de Investigación y Desarrollo/Fondo Nacional de Desarrollo Científico y Tecnológico (ANID/FONDECYT; project no. 1200779). JO acknowledges support from the ANID scholarship ANID-PFCHA/Doctorado Nacional/2020–21200903. The authors thank the reviewers for their thoughtful comments and suggestions.

## Appendix A. Supplementary data

Supplementary data to this article can be found online at <https://doi.org/10.1016/j.soildyn.2021.106866>.

## Data and resources

The unprocessed acceleration time histories are obtained from the Rete Accelerometrica Nazionale (RAN), managed by the Department of Civil Protection (DPC; <http://ran.protezionecivile.it/>, last accessed April 2018) and from the INGV International Federation of Digital Seismograph Networks (FDSN) web service (<http://webservices.rm.ingv.it/>, last accessed April 2018). The processed strong-motion data and station metadata are obtained from the Engineering Strong-Motion (ESM) database (<http://esm.mi.ingv.it>, last accessed April 2018). Figures were created using the Generic Mapping Tools version 4.5.3 [51]. Seismic signal analysis was performed using SAC (Seismic Analysis Code) version 101.6 [52,53].

## Funding

This research did not receive any specific grant from funding agencies in the public, commercial, and not-for-profit sectors.

## CRediT authorship contribution statement

**Javier Ojeda:** Conceptualization, Methodology, Formal analysis, Writing - Review & Editing, Data curation, Visualization. **Aybige Akinci:** Conceptualization, Methodology, Validation, Formal analysis, Investigation, Writing- Original draft preparation. **Elisa Tinti:** Methodology, Formal analysis, Visualization, Writing - Review & Editing. **Sebastian Arriola:** Methodology, Software. **Sergio Ruiz:** Validation, Writing- Reviewing & Editing.

## References

- [1] Scognamiglio L, Tinti E, Casarotti E, Pucci S, Villani F, Cocco M, Magnoni F, Michelini A, Dreger D. Complex fault geometry and rupture dynamics of the mw 6.5, 30 october 2016, central Italy earthquake. *J Geophys Res: Solid Earth* 2018; 123(4):2943–64. <https://doi.org/10.1002/2018JB015603>.
- [2] Malagnini L, Akinci A, Mayeda K, Munafò' I, Herrmann RB, Mercuri A. Characterization of earthquake-induced ground motion from the l'aquila seismic sequence of 2009, Italy. *Geophys J Int* 2011;184(1):325–37. <https://doi.org/10.1111/j.1365-246X.2010.04837.x>.
- [3] Doglioni C. Geological remarks on the relationships between extension and convergent geodynamic settings. *Tectonophysics* 1995;252(1–4):253–67. [https://doi.org/10.1016/0040-1951\(95\)00087-9](https://doi.org/10.1016/0040-1951(95)00087-9).
- [4] Patacca E, Scandone P, Di Luzio E, Cavinato GP, Parotto M. Structural architecture of the central apennines: interpretation of the crop 11 seismic profile from the adriatic coast to the orographic divide. *Tectonics* 2008;27(3). <https://doi.org/10.1029/2005TC001917>.
- [5] Dugdale SK. *Earthquake resistant design of structures*. New Delhi: Oxford university press; 2007.
- [6] Douglas J, Aochi H. A survey of techniques for predicting earthquake ground motions for engineering purposes. *Surv Geophys* 2008;29(3):187. <https://doi.org/10.1007/s10712-008-9046-y>.
- [7] Graves R, Pitarka A. Refinements to the graves and pitarka (2010) broadband ground-motion simulation method. *Seismol Res Lett* 2015;86(1):75–80. <https://doi.org/10.1785/0220140101>.
- [8] Aagaard BT, Graves RW, Rodgers A, Brocher TM, Simpson RW, Dreger D, Petersson NA, Larsen SC, Ma S, Jachens RC. Ground-motion modeling of hayward fault scenario earthquakes, part ii: simulation of long-period and broadband ground motions. *Bull Seismol Soc Am* 2010;100(6):2945–77. <https://doi.org/10.1785/0120090379>.
- [9] Pitarka A, Graves R, Irikura K, Miyakoshi K, Rodgers A. Kinematic rupture modeling of ground motion from the m7 kumamoto, Japan earthquake. *Pure Appl Geophys* 2020;177(5):2199–221. <https://doi.org/10.1007/s0024-019-02220-5>.
- [10] Mai PM, Imperatori W, Olsen KB. Hybrid broadband ground-motion simulations: combining long-period deterministic synthetics with high-frequency multiple s-to-s backscattering. *Bull Seismol Soc Am* 2010;100(5A):2124–42. <https://doi.org/10.1785/0120080194>.
- [11] Mena B, Dalguer L, Mai PM. Pseudodynamic source characterization for strike-slip faulting including stress heterogeneity and super-shear ruptures. *Bull Seismol Soc Am* 2012;102(4):1654–80. <https://doi.org/10.1785/0120110111>.
- [12] Akinci A, Aochi H, Herrero A, Pischiutta M, Karanikas D. Physics-based broadband ground-motion simulations for probable mw=7.0 earthquakes in the marmara sea region (Turkey) physics-based broadband ground-motion simulations for probable mw ≥7.0 earthquakes. *Bull Seismol Soc Am* 2017;107(3):1307–23. <https://doi.org/10.1785/0120160096>.
- [13] Shahjouei A, Pezeshl S. Synthetic seismograms using a hybrid broadband ground-motion simulation approach: application to central and eastern United States. *Bull Seismol Soc Am* 2015;105(2A):686–705. <https://doi.org/10.1785/0120140219>.
- [14] Pischiutta M, Akinci A, Tinti E, Herrero A. Broad-band ground-motion simulation of 2016 amatrice earthquake, central Italy. *Geophys J Int* 2021;224(3):1753–79. <https://doi.org/10.1093/gji/ggaa412>.
- [15] Bouchon M. A simple method to calculate green's functions for elastic layered media. *Bull Seismol Soc Am* 1981;71(4):959–71.
- [16] Hartzell SH, Heaton TH. Inversion of strong ground motion and teleseismic waveform data for the fault rupture history of the 1979 imperial valley, California, earthquake. *Bull Seismol Soc Am* 1983;73(6A):1553–83.
- [17] Hisada Y. An efficient method for computing green's functions for a layered half-space with sources and receivers at close depths. *Bull Seismol Soc Am* 1994;84(5):1456–72.
- [18] Irikura K. Prediction of strong acceleration motion using empirical green's function. In: Proc. 7th Japan Earthq. Eng. Symp. 1986. p. 151–6.
- [19] Hanks TC, McGuire RK. The character of high-frequency strong ground motion. *Bull Seismol Soc Am* 1981;71(6):2071–95.
- [20] Boore DM. Stochastic simulation of high-frequency ground motions based on seismological models of the radiated spectra. *Bull Seismol Soc Am* 1983;73(6A):1865–94.
- [21] Beresnev IA, Atkinson GM. Modeling finite-fault radiation from the  $\omega^n$  spectrum. *Bull Seismol Soc Am* 1997;87(1):67–84.
- [22] Motazedian D, Atkinson GM. Stochastic finite-fault modeling based on a dynamic corner frequency. *Bull Seismol Soc Am* 2005;95(3):995–1010. <https://doi.org/10.1785/0120030207>.
- [23] Otarola C, Ruiz S. Stochastic generation of accelerograms for subduction earthquakes. *Bull Seismol Soc Am* 2016;106(6):2511–20. <https://doi.org/10.1785/0120150262>.
- [24] Dreger DS, Gee L, Lombard P, Murray MH, Romanowicz B. Rapid finite-source analysis and near-fault strong ground motions: application to the 2003 mw 6.5 san simeon and 2004 mw 6.0 parkfield earthquakes. *Seismol Res Lett* 2005;76(1):40–8. <https://doi.org/10.1785/gssrl.76.1.40>.
- [25] Ruiz S, Ojeda J, Pastén C, Otarola C, Silva R. Stochastic strong-motion simulation in borehole and on surface for the 2011 mw 9.0 tohoku-oki megathrust earthquake considering p, sv, and sh amplification transfer functions stochastic strong-motion simulation in borehole and on surface for the tohoku-oki megathrust earthquake. *Bull Seismol Soc Am* 2018;108(5A):2333–46. <https://doi.org/10.1785/0120170342>.
- [26] Aki K, Richards PG. *Quantitative seismology*. 2002.
- [27] Boore DM, Joyner WB. Site amplifications for generic rock sites. *Bull Seismol Soc Am* 1997;87(2):327–41.
- [28] Mai PM, Beroza G. A hybrid method for calculating near-source, broadband seismograms: application to strong motion prediction. *Phys Earth Planet In* 2003; 137(1–4):183–99. [https://doi.org/10.1016/S0031-9201\(03\)00014-1](https://doi.org/10.1016/S0031-9201(03)00014-1).
- [29] Lavechia G, Brozzetti F, Barchi M, Menichetti M, Keller JV. Seismotectonic zoning in east-central Italy deduced from an analysis of the neogene to present deformations and related stress fields. *GSA Bull.* 1994;106(9):1107–20.

- [30] Barchi M, Galadini F, Lavecchia G, Messina P, Michetti A, Peruzza L, Pizzi A, Tondi E, Vittori E. Sintesi delle conoscenze sulle faglie attive in italia centrale: parametrizzazione ai fini della caratterizzazione della pericolosità sismica. 2000. p. 1–45.
- [31] Boncio P, Lavecchia G, Milana G, Rozzi B, et al. Seismogenesis in central apennines, Italy: an integrated analysis of minor earthquake sequences and structural data in the amatrice-campotosto area. *Ann Geophys* 2004;47(6):1723–42.
- [32] Carafa MM, Bird P. Improving deformation models by discounting transient signals in geodetic data: 2. geodetic data, stress directions, and long-term strain rates in Italy. *J Geophys Res: Solid Earth* 2016;121(7):5557–75. <https://doi.org/10.1002/2016JB013038>.
- [33] D'Agostino N. Complete seismic release of tectonic strain and earthquake recurrence in the apennines (Italy). *Geophys Res Lett* 2014;41(4):1155–62. <https://doi.org/10.1002/2014GL059230>.
- [34] Petricca P, Barba S, Carminati E, Doglioni C, Riguzzi F. Graviquakes in Italy. *Tectonophysics* 2015;656:202–14. <https://doi.org/10.1016/j.tecto.2015.07.001>.
- [35] Devoti R, d'Agostino N, Serpelloni E, Pietranonio G, Riguzzi F, Avallone A, Cavalieri A, Cheloni D, Cecere G, d'Ambrosio C, et al. A combined velocity field of the mediterranean region. *Ann Geophys* 2017;60(2):0215. <https://doi.org/10.4401/ag-7059>.
- [36] Amato A, Azzara R, Chiarrabba C, Cimini G, Cocco M, Di Bona M, Margheriti L, Mazza S, Mele F, Selvaggi G, et al. The 1997 umbria-marche, Italy, earthquake sequence: a first look at the main shocks and aftershocks. *Geophys Res Lett* 1998;25(15):2861–4. <https://doi.org/10.1029/98GL51842>.
- [37] Chiaramuce L, Di Stefano R, Tinti E, Scognamiglio L, Michele M, Casarotti E, Cattaneo M, De Gori P, Chiarrabba C, Monachesi G, et al. The 2016 central Italy seismic sequence: a first look at the mainshocks, aftershocks, and source models. *Seismol Res Lett* 2017;88(3):757–71. <https://doi.org/10.1785/0220160221>.
- [38] Herrmann RB, Malagnini L, Munafò I. Regional moment tensors of the 2009 l'aquila earthquake sequence. *Bull Seismol Soc Am* 2011;101(3):975–93. <https://doi.org/10.1785/0120100184>.
- [39] Tinti E, Scognamiglio L, Michelini A, Cocco M. Slip heterogeneity and directivity of the ml 6.0, 2016, amatrice earthquake estimated with rapid finite-fault inversion. *Geophys Res Lett* 2016;43(20):10–745. <https://doi.org/10.1002/2016GL071263>.
- [40] Brune JN. Tectonic stress and the spectra of seismic shear waves from earthquakes. *J Geophys Res* 1970;75(26):4997–5009. <https://doi.org/10.1029/JB075i026p04997>.
- [41] Kausel E, Roësset JM. Stiffness matrices for layered soils. *Bull Seismol Soc Am* 1981;71(6):1743–61.
- [42] Kausel E. Fundamental solutions in elastodynamics: a compendium. Cambridge University Press; 2006.
- [43] Ugurhan B, Askan A, Akinci A, Malagnini L. Strong-ground-motion simulation of the 6 april 2009 l'aquila, Italy, earthquake. *Bull Seismol Soc Am* 2012;102(4):1429–45. <https://doi.org/10.1785/0120110060>.
- [44] Anderson JG, Hough SE. A model for the shape of the fourier amplitude spectrum of acceleration at high frequencies. *Bull Seismol Soc Am* 1984;74(5):1969–93.
- [45] Felicetta C, Mascandola C, Spallarossa D, Pacor F, Hailemikael S, Di Giulio G. Quantification of site effects in the amatrice area (central Italy): insights from ground-motion recordings of the 2016–2017 seismic sequence. *Soil Dynam Earthq Eng* 2021;142:106565. <https://doi.org/10.1016/j.soildyn.2020.106565>.
- [46] Joyner W, Fumal T. Use of measured shear-wave velocity for predicting geologic site effects on strong ground motion. *Proc. of the 8th world conf. On earthquake engineering*, vol. 2; 1984. p. 777–83.
- [47] Boore DM, Thompson EM, Cadet H. Regional correlations of vs 30 and velocities averaged over depths less than and greater than 30 meters. *Bull Seismol Soc Am* 2011;101(6):3046–59. <https://doi.org/10.1785/0120110071>.
- [48] Boore DM. The uses and limitations of the square-root-impedance method for computing site amplification. *Bull Seismol Soc Am* 2013;103(4):2356–68. <https://doi.org/10.1785/0120120283>.
- [49] Ghofrani H, Atkinson GM, Goda K, Assatourians K. Stochastic finite-fault simulations of the 2011 Tohoku, Japan, earthquake. *Bull Seismol Soc Am* 2013;103(2B):1307–20. <https://doi.org/10.1785/0120120228>.
- [50] Bindi D, Pacor F, Luzi L, Puglia R, Massa M, Ameri G, Paolucci R. Ground motion prediction equations derived from the Italian strong motion database. *Bull Earthq Eng* 2011;9(6):1899–920. <https://doi.org/10.1007/s10518-011-9313-z>.
- [51] Wessel P, Smith WH, Scharroo R, Luis J, Wobbe F. Generic mapping tools: improved version released. *Eos Trans Am Geophys Union* 2013;94(45):409–10. <https://doi.org/10.1002/2013EO450001>.
- [52] Goldstein P, Dodge D, Firpo M, Minner L, Lee W, Kanamori H, Jennings P, Kisslinger C. Sac2000: signal processing and analysis tools for seismologists and engineers. In: The IASPEI international handbook of earthquake and engineering seismology. 81; 2003. p. 1613–20.
- [53] Goldstein P, Snook A. Sac availability for the iris community. *Incorporated research Institutions for seismology newsletter*, vol. 7; 2005. UCRL-JRNL-211140).